Ultrasonic Nondestructive Diagnosis of Lithium-Ion Batteries with Multiple Frequencies

Hongbin Sun[a,*], Nitin Muralidharan[a], Ruhul Amin[a], Vivek Rathod[a], Pradeep Ramuhalli[a], Ilias Belharouak[a]

[a]*Oak Ridge National Laboratory, One Bethel Valley Road, Oak Ridge, TN 37830*

Abstract

Accurately estimating of state of charge (SoC) in battery management systems (BMSs) requires the measurement of numerous parameters and advanced algorithms. This work studies multifrequency ultrasonic waves to estimate the SoC of Li-ion batteries by sensing the material changes during charge/discharge. A pouch-type $LiNi_{0.6}Mn_{0.2}Co_{0.2}O_2$ (NMC622)||graphite battery cell is designed and fabricated with a capacity of 2.4 Ah. Different ultrasonic testing setups are explored to determine the optimal testing parameters for the battery. An ultrasonic monitoring system is developed to monitor the battery during charge/discharge at 750 kHz, 1 MHz, and 1.5 MHz. Signal processing algorithms are proposed for extracting three ultrasonic features—amplitude, wave velocity, and attenuation. In a three-cycle test, the amplitude histories do not show clear correlations with the SoC. The wave velocities of all three frequencies have an approximately linear relationship with the SoC, which can be used for SoC estimation. Hysteresis behavior is observed for the wave velocity in terms of a larger slope in the discharge process and velocity drop after a close charge/discharge cycle. The wave attenuation is able to capture the material phase transitions during charge/discharge.

Keywords: lithium-ion battery, state of charge, ultrasonic wave, multiple frequencies, wave velocity, attenuation

2010 MSC: 00-01, 99-00

*Corresponding author

Email addresses: sunh1@ornl.gov (Hongbin Sun), muralidharan@ornl.gov (Nitin Muralidharan), aminr@ornl.gov (Ruhul Amin), rathodv@ornl.gov (Vivek Rathod), ramuhallip@ornl.gov (Pradeep Ramuhalli), belharouaki@ornl.gov (Ilias Belharouak)

1. Introduction

The Li-ion battery is an energy storage system that is widely used in portable electronic devices and electric vehicles. However, Li-ion batteries are extremely complex systems with potential operational safety risks. Therefore, a battery management system (BMS) is required to control the battery operation to optimize the performance, lifetime, and safety. One of the most important features of a BMS is the ability to estimate the state of charge (SoC) [1, 2]. There are many existing SoC estimation methods in the laboratory, such as the coulometric titration technique [3]. However, it is challenging to estimate the SoC of commercial batteries without discontinuing the power supply or destructing the battery structure, especially for online estimation [1]. Existing SoC estimation methods in a BMS include the discharge test method, Ampere-Hour integral (i.e., coulomb counting) method, open-circuit voltage method [4], battery model-based method [5], and machine learning (ML) method [6]. These methods require either a long time to execute and extra hardware or the measurement of extrinsic parameters (e.g., voltage, current, temperature, running time) and advanced algorithms (e.g., the Kalman filter). This type of BMS requires expensive hardware and complex software. An alternative low-cost and simple system is desired for the SoC estimation of Li-ion batteries.

The Li-ion battery is fundamentally a composite material system with multiple layers of electrodes. The mechanical properties of the system evolve during the delithiation and lithiation, such as modulus and density changing at different SoCs. A nondestructive evaluation technique using ultrasound was recently applied for battery SoC estimation. Ultrasonic testing is one of the most widely used techniques for nondestructive evaluation of material properties and structural health monitoring. The stress wave excited by the ultrasonic transmitter propagates in the material and is received by the ultrasonic receiver. The material properties, internal structure, and damage can be accurately evaluated and continuously monitored with the received ultrasonic signal. Therefore, the evolving mechanical properties (e.g., modulus, density, Poisson's ratio) and structure can be monitored via ultrasonic wave propagating through the battery body. The correlation could be built between the ultrasonic parameters and battery SoC. Hsieh et al. [7] first proposed an acoustic (i.e., ultrasonic) wave to measure the SoC and state of health (SoH) on Li-ion 18650 and alkaline LR6 batteries. Experimental results demonstrated that the time of flight (ToF) and ultrasonic signal amplitude had a strong correlation with the battery SoC and SoH.

Davies et al. [8] further investigated the changes of ToF and signal amplitude during the charge/discharge of a Li-ion pouch cell and discussed the modulus change of the anode (graphite) and cathode ($LiCoO_2$). Hysteresis behavior in the ultrasonic wave ToF was found during any charge/discharge cycle. Finally, an ML model was built to predict the SoC with ToF, signal amplitude, and input voltage as the model input. A high-frequency (2.25 MHz) ultrasonic wave was used in previous works to achieve high-sensing sensitivity. In contrast, studies using relative low-frequency ultrasonic waves were reported for battery SoC prediction.

Gold et al. [9] discovered that the arrival time of a 200 kHz ultrasonic wave through the thickness of a pouch cell was linearly related to the battery SoC. Relatively low frequency is used because the high-frequency ultrasonic wave has an attenuation so high that the received signal amplitude would be too small. Ladpli et al. [10] proposed an ultrasonic guided wave method for SoC and SoH estimation. The pouch cell was treated as a multiplayer wave guide, and the ultrasonic guided wave of 100–200 kHz was propagated in the battery. The battery SoC and SoH were predicted using ML models with ToF and signal amplitude as the model input. The work also found some nonlinear features on the ToF and signal amplitude, which was induced by the intercalation staging in the graphitic anode. The ultrasonic method was also studied in other works for SoC and SoH prediction of Li-ion pouch cells [11, 12, 13]. Based on a similar mechanism, Bommier et al. [14] used ultrasound to detect SEI formation and capacity degradation of Si/graphite composites in a full cell setting. Zhang et al. [15] proposed an in situ ultrasonic measurement technique to monitor the NMC622 and graphite drying process with ultrasonic attenuation. The ultrasonic inspection technique can also detect defection for Li-ion batteries. Li and Zhou [16] utilized air-coupled ultrasonic wave for stomata defect detection, and Robinson et al. [17] identified the designed missing half of the negative-electrode layer with the ultrasonic signal amplitude.

This paper presents an experimental study of ultrasonic diagnosis of the Li-ion battery at multiple frequencies. While the previous studies focused on applying the ultrasonic technique for SoC estimation, this work emphasized the fundamental experimental study of ultrasonic testing for Li-ion batteries, including the optimal testing setups, algorithms of ultrasonic feature extraction, and sensitivity of these features. Most studies used one frequency ultrasonic wave for measurement. This work deployed an ultrasonic testing system at multiple frequencies for monitoring battery charge/discharge. The results from multi-frequency sensing could provide more comprehensive information than one frequency to understand the material changes of delithiation and lithiation. The proposed method was validated on Li-ion pouch cells, and the ultrasonic parameters of amplitude, velocity, and attenuation were correlated with the battery SoC.

2. Ultrasonic Nondestructive Evaluation of Li-Ion Batteries

The ultrasonic measurement technique can provide a nondestructive method for evaluating the material properties. Figure 1 provides a schematic diagram of the ultrasonic measurement on a Li-ion pouch cell. The ultrasonic transmitter is excited by an ultrasonic pulser and will transmit stress waves into the pouch cell. The ultrasonic wave will experience transmission, reflection, and attenuation when propagating through the multilayer that comprises positive and negative electrodes and finally be received by the ultrasonic receiver. In Figure 1, two transducers are at the two side surfaces of the battery to create the through-transmission model. For pulse-echo mode, only one transducer is used as both transmitter and receiver. For the through-transmission mode, the first arrival signal propagates a distance of the thickness. Once the first arrival ToF

is extracted, the ultrasonic velocity can be obtained. In a homogeneous material, the propagation velocity of the longitudinal (i.e., compressional) wave is associated with the material elastic modulus E, density ρ, and Poisson's ratio ν as:

$$V_L = \sqrt{\frac{E(1-\nu)}{\rho(1+\nu)(1-2\nu)}}. \tag{1}$$

For a Li-ion battery with multilayer electrodes, the average longitudinal velocity is related not only to the elastic properties (e.g., modulus, density, Poisson's ratio) of each layer but also to the interface conditions of adjacent layers. In the charge process, the cathode (e.g., $LiCoO_2$) elastic modulus will decrease, and the anode (e.g., graphite) elastic modulus will increase [18, 19], while both densities will decrease. The average wave velocity through the battery electrodes is affected by the combinations of these parameters.

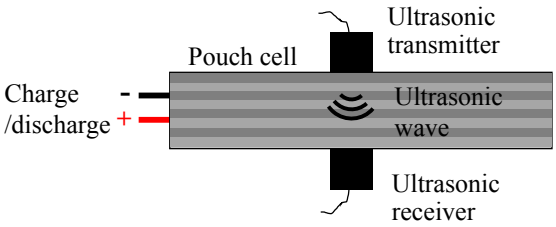

Figure 1: Concept of ultrasonic testing on a Li-ion battery.

Another basic ultrasonic feature is wave attenuation, which represents how much the wave amplitude diminishes when propagating. As the wave propagates through battery electrodes, several factors will contribute to wave attenuation. First, the reflection occurs at the interfaces of adjacent layers. Then, the propagating longitudinal wave may convert to the shear wave, which will also cause attenuation. Because the electrode layer is a composite material, the stress wave may be scattered by its complex internal structure. Part of the energy will be absorbed by the electrode layers and converted to other energy forms. In addition to these, the beam spreading and transducer coupling also contribute to the total attenuation in the received ultrasonic signal. The amplitude of the received signal can be expressed as:

$$A = A_0 e^{-\alpha z}, \tag{2}$$

where A_0 is the original amplitude, and A is the attenuated amplitude after propagation distance z. α is the attenuation coefficient with a unit of Neper per meter, which describes the total attenuation. When the elastic properties of the cathode and anode layers change in the charge/discharge process, the reflection and transmission coefficients also change if the wave propagates from one layer to another layer because of the changing acoustic impedance of these layers. The energy absorption of these layers will change accordingly. The interface bonding condition between adjacent layers will vary during the charge/discharge processes,

which will contribute to the change of wave attenuation. Therefore, the wave attenuation variations during charge/discharge will be a combined effect of the material and structural change. Previous studies used maximum amplitude or total energy to characterize the attenuation of waves transmitting through the battery. However, amplitude and total energy are largely affected by the initial transmitting energy and the transducer coupling condition. The attenuation is analyzed in the frequency domain to eliminate the dispersion effect in this work. The attenuation due to beam spreading is corrected so that the attenuation obtained is related only to the material property changes.

3. Experimental Details

3.1. Battery Fabrication

The selected battery chemistry comprised a $LiNi_{0.6}Mn_{0.2}Co_{0.2}O_2$ (NMC622) cathode, graphite carbon anode, and Gen-2 electrolyte packaged with aluminum laminate. The cathode was NMC622 [90%/5% Polyvinylidene Fluoride (PVDF)/5% carbon black] with a total material loading of 14.2 mg/cm^2 per side of electrode. The total thickness of the double-sided coating was around 122 μm with 15 μm aluminum foil. The anode was graphite (Superior SLC1520T 92%/6% PVDF/2% carbon black) with a total material loading of 7.85 mg/cm^2 per side of electrode. The thickness of the double-sided coating was around 115 μm with 10 μm copper foil. The cathode and anode were both calendared to 35% porosity. The negative/positive (N/P) ratio was set at 1.1.

The selection of this chemistry was driven by (1) similarity to typical chemistry used in EV batteries, including those targeted for second-life applications; (2) the ability to produce multiple batteries that have nearly identical properties and are spatially uniform in material properties across the cell; (3) well-understood changes in chemistry and physical properties with repeated charge-discharge cycles; (4) cycling with the standard cell voltage range of 2.5 to 4.5 V as a practical application; and (5) considering practical SoC and discharge. The pouch cell had 13 double-sided cathodes, 12 double-sided anodes, and two single-sided anodes with 11 g of Gen-2 electrolyte filled. The total thickness of the cell was 4.4 mm, including the separator and pouch material, and the total capacity was around 2.6 Ah. The cells were fabricated at Oak Ridge National Laboratory (ORNL). Before the ultrasonic testing, the cells were slowly charged and discharged (C/10 rate) in the formation, formed gas was removed, and the cell was resealed. The initial material characterization of the cathode active material and the assembled electrodes has been added in the supporting information as Figure S1 including scanning electron micrographs in both top view and cross-section and a X-ray diffractogram of the powders. The electrochemical performance assessment of the same batch Li-ion battery is shown in Figure S2 of the supporting information.

3.2. Ultrasonic Test Setup

High-frequency transducers of 1–5 MHz were mostly used for ultrasonic testing of Li-ion batteries [20, 7, 8, 21, 22, 13]. High-frequency ultrasonic waves have a smaller wavelength and are more sensitive to the internal material change of battery than low-frequency waves. Furthermore, high-frequency transducers can be deployed on small-package batteries with micro-electromechanical system piezoelectric transducers [8]. Low-frequency ultrasonic waves around 200 kHz were also deployed in some works [9, 10] because of their low wave attenuation. In most works, only one frequency of a longitudinal wave was used. This work studied different frequencies of ultrasonic waves to monitor batteries' charge/discharge processes. Four candidate types of transducers were selected: 1 and 2.25 MHz longitudinal transducers (Olympus V103 and C106) and 1 and 2.25 MHz shear transducers (Olympus V153 and V154).

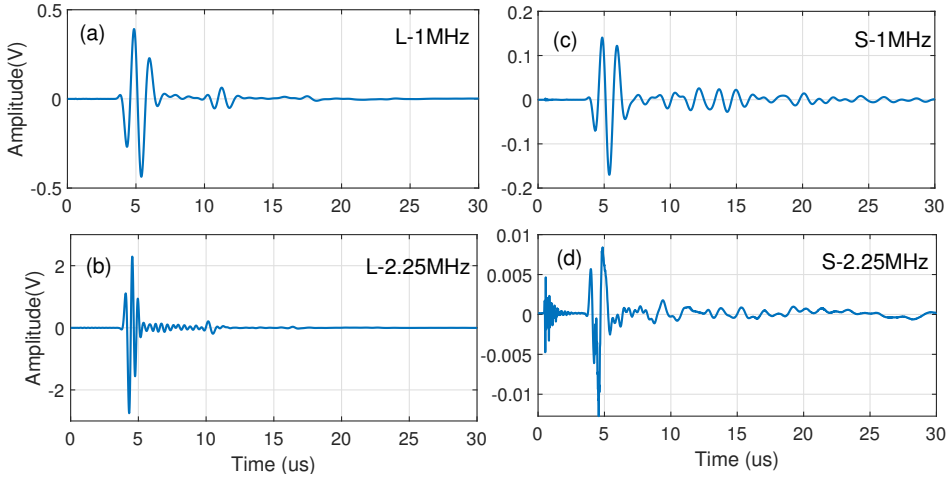

Figure 2: Ultrasonic signals on the Li-ion battery from (a) longitudinal transducer 1 MHz (L-1MHz), (b) longitudinal transducer 2.25 MHz (L-2.25MHz), (c) shear transducer 1 MHz (S-1MHz), and (d) shear transducer 2.25 MHz (S-2.25MHz).

Figure 2 shows the ultrasonic signals collected on the battery using the four pairs of transducers when the battery was not in charge/discharge. Both the signals from L-1MHz and L-2.25MHz had a clear first arrival echo and second reflected echo. The wave attenuation can be calculated by using these two echoes. The amplitude of the reflected echo in the signal of L-2.25MHz, shown in Figure 2(b), was relatively small because of the high attenuation. The signal of the S-1MHz had a reasonable amplitude, but the dominant part of the signal was still the longitudinal wave rather than the shear wave. The signal of the S-2.25MHz showed a very weak signal. Therefore, only the two longitudinal transducers were selected, and the two shear transducers were not used in this work.

The selected L-1MHz and L-2.25MHz transducers were placed at the center position on the battery side surface, and a 3D printed holder was used to ensure that the transmitter and receiver had an accurate alignment on the two side surfaces of the battery. Vaseline was used as the couplant for the longitudinal

transducers because it would not dry out during a long-term test. The transmitters and receivers were fixed with C-clamps to ensure a stable contact between the transducers and the battery. Because the transducers selected were broadband transducers, the L-1MHz and L-2.25MHz transducers were also excited at lower frequencies in addition to their center frequencies to explore the test sensitivity of different frequencies. After several trial tests, the excitation frequencies and corresponding excitation voltage for the two transducers were selected and summarized in Table 1.

Table 1: Selected ultrasonic transducer pairs and corresponding excitation frequencies.

Channel	1	2	3
Transducer	L-1MHz	L-1MHz	L-2.25MHz
Excitation frequency	750 kHz	1.0 MHz	1.5 MHz
Excitation voltage	120 V	120 V	120 V

Different excitation waveforms were explored, including a short-duration pulse, a square wave, and different cycles of the tone burst. The energy of the short-duration pulse and the square wave was unable to generate enough energy for the wave to propagate through the battery. A one-cycle tone burst experienced the same problem. For a three-cycle tone burst, the first echo in the signal was overlapped with the reflected echo, which was nonviable for the attenuation calculation. Therefore, a two-cycle tone burst was finally selected as the excitation waveform. An excitation voltage of 120 V was used to achieve a reasonable signal-to-noise ratio and avoid transducer overload. The battery was also tested in a pule-echo mode with only one transducer for transmitting and receiving. However, the first and the second echo had low amplitude in the received signals because their propagation distances were longer than those in the through-transmission mode.

3.3. Ultrasonic Monitoring System for Charge/Discharge Test

The pouch-type battery cells were tested by using an ultrasonic testing system. The system used two pairs of transducers with transmitters and receivers. The ultrasonic transmitters were driven by a function generator (Agilent 81150A) and an amplifier (Ritec GA-2500A) with a two-cycle tone burst. The ultrasonic wave was transmitted into the battery from one side surface, and the signal was received by the corresponding receiver on the other side surface. The received ultrasonic signals were collected using an oscilloscope (NI PXIe-5122) with a sampling rate of 100 MS/s and 100 times average to increase the signal-to-noise ratio. A multiplexer (Keysight DAQ970A) was used to switch between the two pairs of transducers. Meanwhile, the battery temperature and air temperature were measured using three Type-T thermocouples. The ultrasonic signals and temperature data were collected simultaneously every 2 min during the battery charge/discharge. The battery cell was charged and discharged using a potentiostat (Biologic, SP-200) with a C/10 rate

and a constant current (240 mA). Figure 3 shows the voltage, current, and SoC histories of a three-cycle charge/discharge with a C/10 rate. The charge/discharge voltage ranged from 3.0 to 4.2 V with a constant current of 240 mA. Each charge/discharge cycle was 20 h.

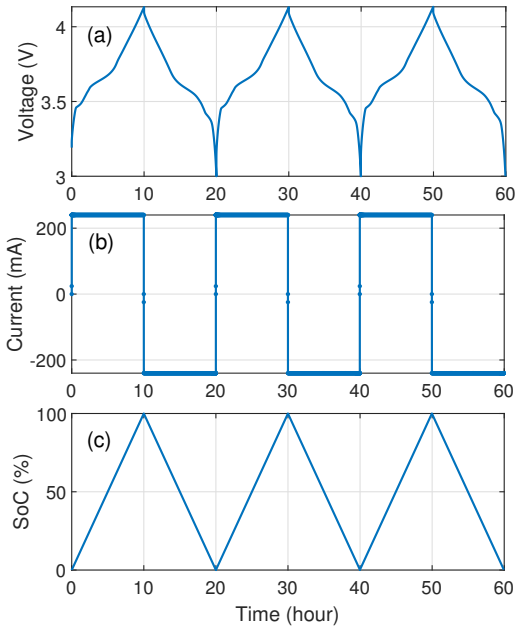

Figure 3: Battery charge/discharge profile: (a) voltage history, (b) current history, and (c) SoC history.

4. Ultrasonic Wave Features Analysis

Three ultrasonic wave features were extracted from the ultrasonic signals: signal amplitude, wave velocity, and wave attenuation. The peak-to-peak amplitude was used as signal amplitude. The wave velocity and wave attenuation extraction require complicated signal processing algorithms, as discussed in this section.

The ultrasonic wave velocity history was extracted from the monitoring signals in terms of relative velocity change and absolute velocity. The maximum velocity change during the battery charge/discharge was on the order of 1%, and such a small velocity change cannot be captured by using the conventional method with the first arrival time. Therefore, a stretching technique from the coda wave interferometry was adopted to analyze the relative velocity change. The technique can achieve a precision of 10^{-5} of relative velocity change [23], and the precision still can be improved with a higher signal sampling rate. The stretching technique was proposed by Lobkis and Weaver [24], and it compares the reference signal φ and

the perturbed signal φ' and computes the cross-correlation coefficient CC(ε) as:

$$CC(\varepsilon) = \frac{\int_{t_1}^{t_2} \varphi'[t(1-\varepsilon)]\varphi(t)dt}{\sqrt{\int_{t_1}^{t_2} \varphi'^2[t(1-\varepsilon)]dt \int_{t_1}^{t_2} \varphi^2(t)dt}}. \tag{3}$$

The stretching factor ε_{max}, which maximizes the cross-correlation coefficient CC, represents the relative ToF change $\frac{\delta t}{t}$. When the wave propagation distance is constant, the relative velocity change $\frac{dv}{v}$ equals $-\frac{\delta t}{t}$. In this work, the battery and transducers were clamped, and the authors assumed a constant distance between the two transducers. The analysis always used the first signal at 0% SoC as the reference signal, and the relative velocity change was calculated by comparing every signal with the reference signal. Therefore, the calculated relative velocity change for the 100% SoC was +0.79%, which indicates that the velocity at 100% is 1.0079 times that of the velocity at 0% SoC. The absolute velocity history was analyzed by using the absolute velocity $v_1 = d/t_1$ of the first signal (i.e., reference signal) and the relative velocity history $(\frac{dv}{v})_i$. The first arrival time t_1 of the first signal was captured using the Akaike information criterion picker [25]. The absolute velocity history can be presented as:

$$v_i = \frac{d}{t_1}\left[1 + (\frac{dv}{v})_i\right], \tag{4}$$

where d is the battery thickness, and $(\frac{dv}{v})_1 = 0$ for the first signal.

Wave attenuation was analyzed with the first arrival echo packet and the reflected echo packet. Figure 2(a) plots the time-domain signal from the L-1MHz transducers at 0% SoC. The signal had multiple echo packets, and only the first and second echo packets were used for the attenuation calculation. The first and second echoes were windowed at [3 μs, 8.5 μs] and [8.5 μs, 14 μs], respectively, and then transformed to the frequency spectra using fast Fourier transform. The experimental attenuation was calculated by taking the ratio between the two amplitude spectra $X_1(f)$ and $X_2(f)$ as:

$$Att(f) = -20\log\left[\frac{X_2(f)}{X_1(f)}\right], \tag{5}$$

where $Att(f)$ represents the attenuation at different frequencies. Ultrasonic attenuation estimation typically requires a correction for beam-spreading with the amplitudes $X_n(f)$ in Eq. (5) corrected as [26]:

$$X_{n,corrected} = X_n(f)/D(x_n, \omega), \tag{6}$$

where the diffraction coefficient $D(x_n, \omega)$ is propagation distance- and frequency-related as:

$$D(x_n, \omega) = 1 - e^{-i(kr^2/x_n)}\left[J_0(\frac{kr^2}{x_n}) + iJ_1(\frac{kr^2}{x_n})\right]. \tag{7}$$

Here, x_n is the propagation distance of the n^{th} echo, ω is the angular frequency, J_0 and J_1 are the Bessel functions of the first kind, k is the wave number, and r is the transducer radius (6.35 mm for all transducers in this work).

5. Results and Discussion

5.1. Wave Velocity History

The velocity histories were analyzed by using the stretching technique [24] and are plotted in Figures 4(a)–(c). The wave velocity was represented in the percentage change of velocity denoted as the relative velocity change in the left axes. The ultrasonic signal at time zero was used as the reference with its relative velocity change as 0%. All three relative velocity change histories had the same trend with the SoC history with increasing velocity in the charge process and decreasing velocity in the discharge process. Because the graphite has a lower volumetric specific capacity than the NMC622 in the material level [27], the anode graphite has a larger volume in the cell and controls the overall wave propagation time and velocity. The modulus of the graphite increases in the charge process, causing a higher velocity and decreases in the discharge process, which results in a lower velocity. The velocity history of 1.5 MHz had the largest velocity change (1.3%) at full charge, indicating that it was most sensitive to the battery structural or material change during charge/discharge. The absolute wave velocity for 1.5 MHz was estimated to be 1,536 m/s at time zero with 0% SoC in the right axis. At full charge, the wave velocity was 1,556 m/s with a velocity change of 20 m/s. Such a small velocity change cannot be detected by the conventional ultrasonic method, which is why the stretching technique was used.

The correlation curve between the wave velocity of 1.5 MHz and the SoC is plotted in Figure 4(d). The wave velocity histories of 750 kHz and 1 MHz were not presented here because they had results very similar to those of the 1.5 MHz history but showed smaller sensitivity than SoC. The three cycles of the 1.5 MHz correlation curves were represented in black, blue, and red. The wave velocity had an approximately linear relationship with the SoC for the charge and discharge processes for each cycle. In the first cycle, the slope was fitted to be 0.20 m/s per percent SoC with $R^2 = 0.97$ for the charge curve and 0.22 m/s per percent SoC with $R^2 = 0.98$ for the discharge curve. The second and third cycles had similar slopes for the charge (0.20 m/s per percent SoC and 0.21 m/s per percent SoC) and the discharge (0.22 m/s per percent SoC and 0.23 m/s per percent SoC) processes. A hysteresis loop existed for all three charge/discharge cycles, which indicates that the electrochemical reaction in the battery was not fully reversible. The discharge process always had a slightly larger slope than that of the charge process. The hysteresis degree of ultrasonic velocity should be related to the battery charge/discharge rate and SoH. Kim et al. [22] reported a larger hysteresis loop with increasing charge/discharge cycles. Another noticeable behavior was that the wave

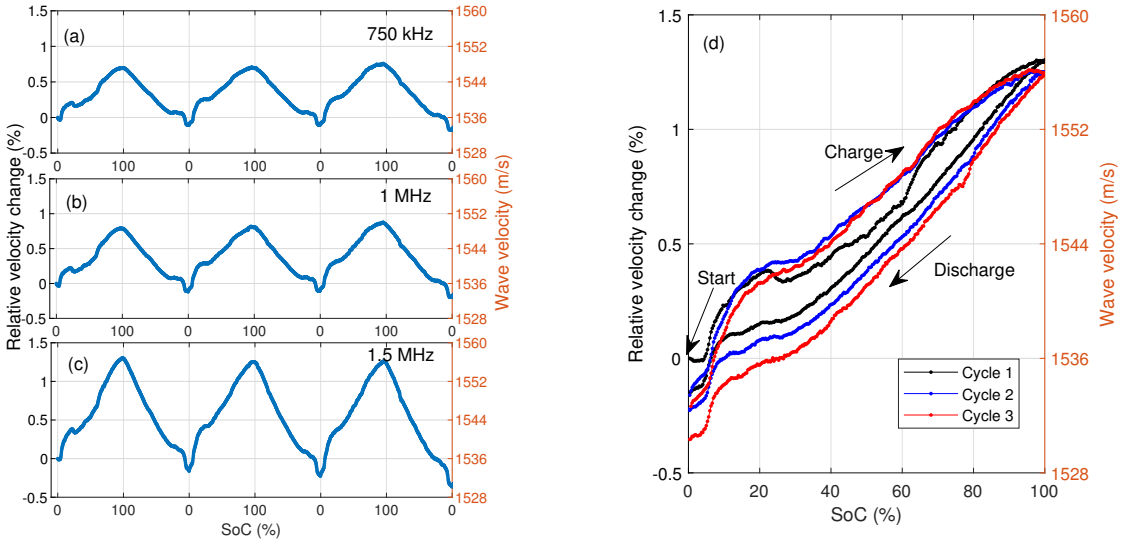

Figure 4: Velocity history of (a) 750 kHz, (b) 1 MHz, and (c) 1.5 MHz. (d) Correlation between the velocity history of 1.5 MHz and SoC. The left y-axis is the relative velocity change (unit percent) and uses the first signal at time zero as the reference. The right y-axis is the absolute wave velocity with a unit of meter per second.

velocity dropped after each charge/discharge cycle, and the final change was -0.354% (1,530 m/s) after three cycles. This behavior was also reported in Davies et al. [8].

To study the temperature effect on the wave velocity, ultrasonic signals were collected when the battery experienced temperature changes in the lab environment with a very slow temperature change rate (0.8°C in 24 h). The battery was considered in thermal equilibrium, and surface temperature was used to represent the global battery temperature. Figure 5(a) shows the velocity change history from 24.4 to 25.2°C at initial 0% SoC. The velocity change had a strong linear relationship (high R^2) with the temperature, and the fitted slope was denoted as the temperature effect coefficient k, which was 4.6 m/s/°C. The test was repeated at five different SoCs (0% $\rightarrow$ 50% $\rightarrow$ 100% $\rightarrow$ 50% $\rightarrow$ 0%), and the coefficient k is plotted at five SoCs in Figure 5(b). The five coefficients were verified in repeated tests. The coefficient k became smaller at higher SoCs and reached 3.11 m/s/°C at full charge. In the discharge process, the coefficient increased and returned to 4.60 m/s/°C at full discharge. The battery wave velocity was more sensitive to the temperature change at a lower SoC. The two coefficients at 50% SoC did not match the charge and discharge processes, indicating that the battery elastic properties differed at these two points. After another 16 charge/discharge cycles, the five coefficients were measured again, and these coefficients were found to have become smaller. Therefore, the temperature effect on the wave velocity is related to both SoC and SoH.

The temperature effect coefficients for the five SoCs were used to compensate the correlation curve between the wave velocity and SoC in Figure 4. Figure 5(c) plots the temperature history over the three charge/discharge cycles. Temperature compensation used the temperature at time zero as the reference

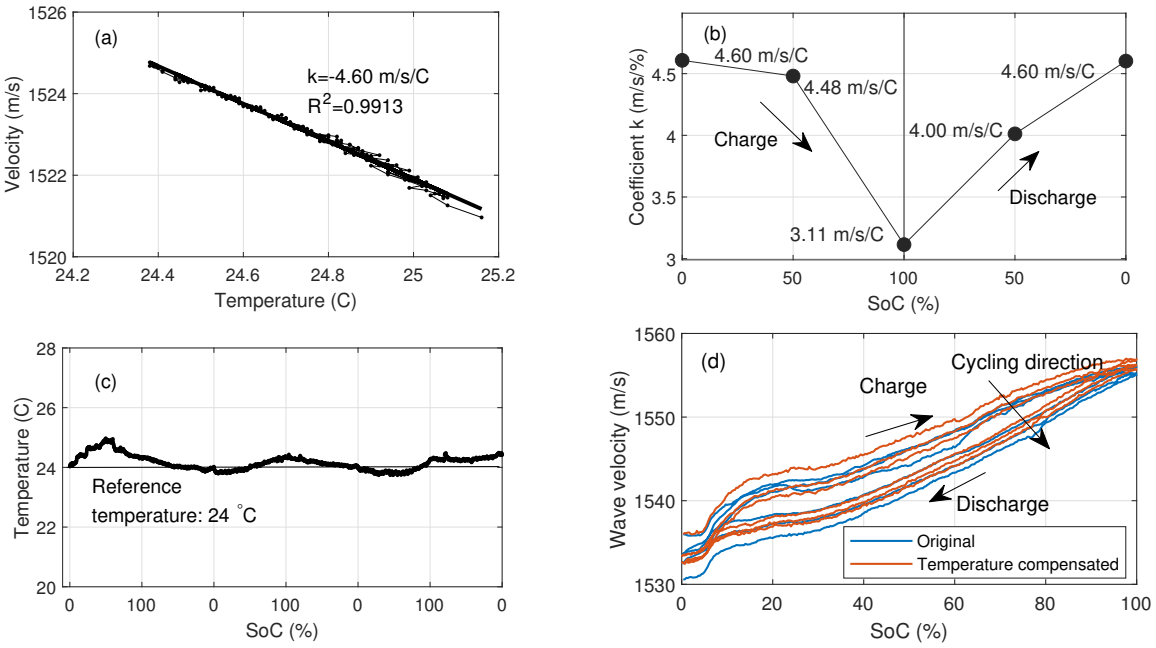

Figure 5: (a) The velocity change at different temperatures for 0% SoC. (b) The temperature effect coefficient k for five SoCs. (c) Battery temperature history during the three-cycle charge/discharge. (d) The velocity change history after temperature compensation.

(24°C). Figure 5(d) presents the correlation curve between relative velocity change and SoC before (blue) and after (red) temperature compensation. With compensation, the slope of the linear relationship between velocity and SoC had only a minor change, which can be ignored. The new correlation curve was squeezed, unlike the original curve. The velocity drop after each charge/discharge cycle became smaller, which indicates that the velocity drop after each cycle was caused by both temperature effect and material hysteresis.

5.2. Wave Attenuation History

The wave attenuations for the three frequencies—750 kHz, 1 MHz, and 1.5 MHz—were analyzed and are plotted in Figure 6(a). The 1 and 1.5 MHz attenuation curves both showed increasing attenuations in the charge process and decreasing attenuations in the discharge process. However, the 750 kHz curve had an opposite trend. One possible explanation is that the 750 kHz wave is more sensitive to the material change of one electrode, whereas the other two frequencies are more sensitive to the material change of the other electrode. The attenuation curves were correlated with the SoC history in Figure 6(b) for the three frequencies. In the figure, the 1 and 1.5 MHz attenuation curves showed positive correlations with SoC, whereas the 750 kHz attenuation curve had a negative correlation with SoC. The attenuation of 750 kHz was the most sensitive to SoC with 2 dB total attenuation change, whereas the other two attenuations had only 1 dB change from 0 to 100% SoC. The 1 and 1.5 MHz attenuation curves both had inflection points

around 63–64% SoC, which did not occur in the 750 kHz attenuation curve. All three correlation curves had local attenuation peaks around 4.7% SoC. When the SoC was near 0%, the modulus of the cathode was at its maximum, the modulus of the anode was at its minimum, and the largest impedance difference was between the anode and cathode. The attenuation due to impedance mismatch contributed more to the total attenuation, causing a local attenuation surge.

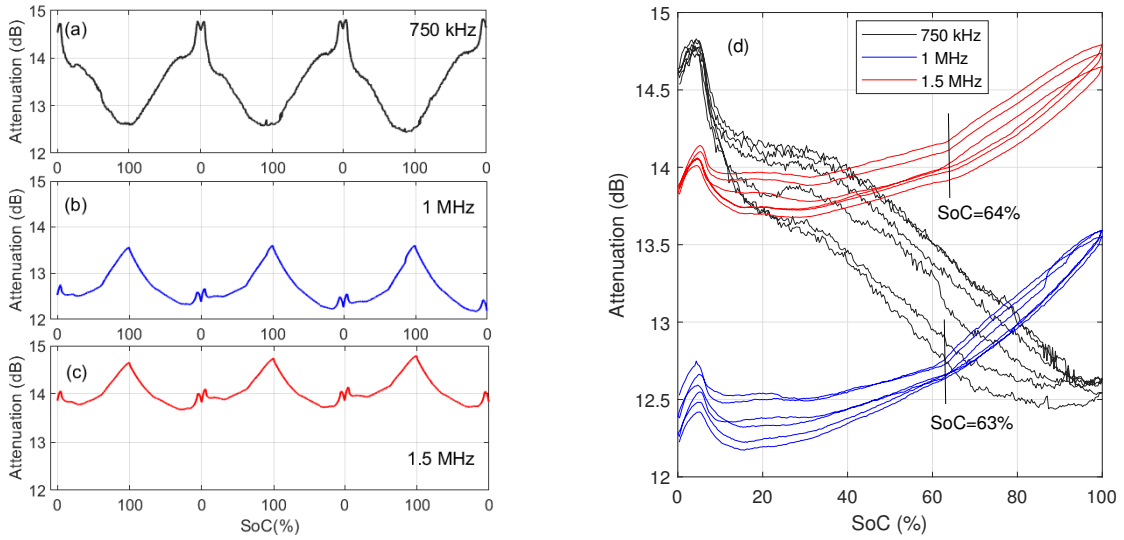

Figure 6: Ultrasonic Wave attenuation histories of (a) 750 kHz, (b) 1 MHz, and (c) 1.5 MHz. (d) Correlation between attenuation history and SoC for the three frequencies.

The differential capacity (dQ/dV) curve from the differential capacity analysis (DCA) and the attenuation of 1.5 MHz of the second cycle are plotted in Figure 7 with the blue curve for the charge process and red for the discharge process. In Figure 7(a), the cell exhibited two redox peaks at 3.46 V (c2) and 3.64 V (c3) on the charge curve and two peaks at 3.40 V (d2) and 3.59 V (d3) on the discharge curve. The first peak on the charge curve started from point c1. The corresponding attenuation for c1 was a local maximum attenuation Ac1 in Figure 7(b) followed by attenuation decreasing to Ac2. At this point, the dQ/dV showed the first peak c2, representing the Li intercalation into the graphite anode ($C_6 \rightarrow LiC_x$). The second peak was c3, which was caused by the phase transition from a hexagonal to a monoclinic (H1→M) lattice of the NMC622 [28, 29]. The corresponding attenuation for c3 was Ac3. Between Ac2 and Ac3, the attenuation was relatively constant, which indicates that the material change in this period was relatively small. At c4, the corresponding attenuation is Ac4, which was the inflection point in Figure 6(b). After Ac4, the attenuation had a linear relationship with the battery potential. During discharge, the attenuation change was largely reversible with attenuation Ad4, Ad3, Ad2, and Ad1 for corresponding points d4, d3, d2, and d2. Although the wave attenuation did not show a linear relationship with the SoC, it still captured the details of the material phase transitions in the delithiation and lithiation processes. The ultrasonic attenuation is

usually affected by the lattice parameter in metallic materials [30], therefore, it may be able to be correlated to change of the lattice parameters (especially c) of the cathode and anode, which was studied in previous literature [31, 32, 33].

Previously, our group has exhaustively investigated the various structural transitions that occur during the electrochemical charge/discharge of the NMC 622 system [34, 35, 36, 37, 38]. Additionally, there is a plethora of manuscripts available in literature on the same battery chemistry which we have employed here. From this, we can identify the phase transitions occurring in this system with a good level of certainty. The NMC 622 cathode material undergoes structural transitions from hexagonal H1 to monoclinic M, (3.4 V - 3.6 V) followed by the monoclinic phase converting to a hexagonal H2 phase beyond 3.6 V. The graphite, on the other hand, undergoes staging phenomena in this voltage window which has also been extensively reported in literature. Additionally, greater accuracy in correlating the phase transitions with the attenuation curve can be achieved by performing combined operando X-ray powder diffraction (XRD) (using hard X-rays from Mo or Ag sources) and ultrasonic NDE measurements on thin lithium-ion battery pouch cells (<5 anode and cathode layers) which would be disseminated as a result of a follow-up study presently underway.

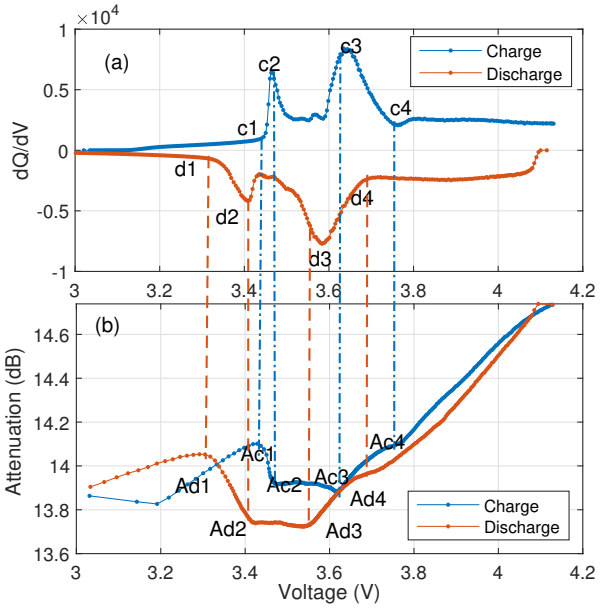

Figure 7: Second charge cycle: (a) differential capacity analysis curves and (b) attenuation curves of 1.5 MHz at different voltages.

5.3. Ultrasonic Signal Amplitude

Ultrasonic signals were collected for a three-cycle charge/discharge test. Peak-to-peak amplitudes were extracted from the ultrasonic signals. The amplitude histories are plotted in Figure 8 along with the SoC history. The signal amplitude histories of 750 kHz and 1 MHz did not show a clear correlation with the

SoC history, and the amplitude variations during charge/discharge were less than 0.1 V. The could be due to the low sensitivity of the 1 MHz transducer used. Only the amplitude history of the 1.5 MHz had a good correlation with the SoC history in Figure 8(c). The amplitude increased in the charge process and decreased in the discharge process, which was caused by the increasing modulus in the charge process and the decreasing modulus in the discharge process. The amplitude history of one charge/discharge cycle was very similar to the result obtained in Davies et al. [8]. The amplitude showed shows a nonmonotonic behavior with initially increasing until 63.5% SoC. After that, the amplitude rapidly decreased. The trend was very similar to change of the c lattice parameter in the charge process reported in literature [31, 32]. The discharge process showed a symmetric trend to the curve of the discharge process with peak amplitude at 72.5%. Between 4 and 14%, both the charge and discharge processes showed a fast-changing stage, indicating a significant structure or material change in this period. At 4% in both the charge and discharge process, local minima were in the amplitude history, which matched the local maximum attenuation at around 4% SoC in Figure 6(d). The amplitude variation during charge/discharge is a combined effect of multiple factors. In the charge process, the increasing average modulus will enhance the received signal with a higher amplitude. On the other side, the wave attenuation also increases, which attenuates the signal amplitude. Therefore, the signal amplitude is unsuitable for characterizing the SoC.

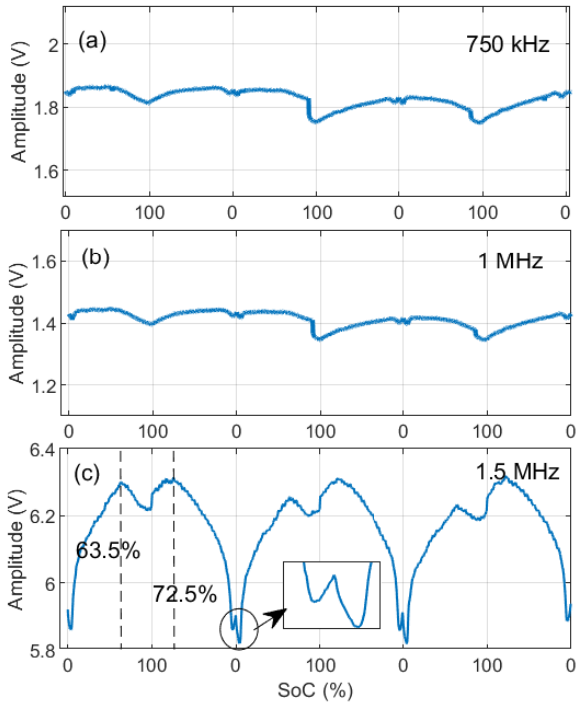

Figure 8: Ultrasonic signal amplitude histories from the transducers of (a) 750 kHz, (b) 1 MHz, and (c) 1.5 MHz.

6. Conclusions and discussions

In this work, multifrequency ultrasonic waves were used to monitor the charge/discharge process of Li-ion batteries. A pouch-type battery cell was designed and fabricated with a NCM622 cathode and graphite anode. Different setups for ultrasonic battery testing were explored to determine the optimal transducer type, frequency, excitation waveform, couplant, and testing mode. Finally, a multifrequency ultrasonic system was developed with 1 and 2.25 MHz longitudinal transducers to monitor the charge/discharge process of the battery with a C/10 rate. Signal processing algorithms were proposed to analyze the velocity change and attenuation in the charge/discharge test. Ultrasonic wave features—including signal amplitude, wave velocity, and wave attenuation—were extracted to correlate with the battery SoC. This paper discusses the results of the three-cycle charge/discharge test in detail, and these results were also verified in several repeated tests (see Figure S3-S6 in the supporting information) on the same battery and another battery from the same fabrication batch.

Only the signal amplitude of 1.5 MHz is sensitive to the battery SoC change and it shows consistency with results in the literature. By comparing the amplitude history with the attenuation history, the authors confirmed that the amplitude is simultaneously affected by the material modulus and the acoustic attenuation. However, these two have opposite trends during the charge/discharge. Therefore, the amplitude is not suggested to characterize the battery SoC in this work.

The velocities of all three frequencies show a positive linear relationship with the battery SoC. The velocity increases in the charge process and decreases in the discharge process, indicating the rising and descending average modulus in the charge and discharge processes, respectively. The velocity of 1.5 MHz is the most sensitive to the battery SoC, and the slope of the linear relationship is around 0.2 m/s per percent SoC. For each cycle, the slope of the discharge process is slightly larger than that of the charge process, which showed a hysteresis behavior here. Another hysteresis behavior is that the velocity dropped after each charge/discharge cycle, which may provide a possible path to characterizing the SoH of the battery. The temperature effect on the wave velocity was also studied at different SoCs. However, it is only the environmental temperature effect. In the future work, higher charge/discharge rates will be used to study the effect of temperature variations caused by fast charge/discharge.

The attenuations of all three frequencies are sensitive to the battery SoC change. The 750 kHz attenuation is the most sensitive to battery SoC and has an opposite trend with the SoC. The 1 and 1.5 MHz attenuations are less sensitive but have similar trends with the SoC. One possible explanation is that the first attenuation (750 kHz) was sensitive to the material change in the cathode, whereas the other two attenuations (1 and 1.5 MHz) were sensitive to the material change in the anode. Therefore, multi-frequency ultrasonic waves are suggested for monitoring the material changes of battery charge/discharge. The attenuation did not not show a linear relationship with the SoC, but captured phase transitions of NMC622 in the attenuation

histories of 1 and 1.5 MHz. Because the wave attenuation is very sensitive to the material changes, it has a great potential for estimating the SoH of batteries.

CRediT Authorship Contribution Statement

Hongbin Sun: Conceptualization, Methodology, Investigation, Experiment, Formal analysis, Software, Writing - Original Draft, Writing - Review & Editing. **Nitin Muralidharan:** Fabrication, Experiment, Writing - Original Draft, Writing - Review & Editing. **Ruhul Amin:** Fabrication, Experiment, Writing - Original Draft, Writing - Review & Editing. **Vivek Rathod:** Writing - Review & Editing. **Pradeep Ramuhalli:** Conceptualization, Methodology, Writing - Review & Editing, Project administration, Supervision. **Ilias Belharouak:**Writing - Review & Editing, Project administration, Supervision.

Declaration of Competing Interest

The authors declare that they have no known competing financial interests or personal relationships that could have appeared to influence the work reported in this paper.

Acknowledgments

This work was supported by the Titan Advanced Energy Solutions and the National Renewable Energy Laboratory through the US Department of Energy Lithium-Ion Battery Recycling Prize. Kelsey Livingston is appreciated for her work on the battery fabrication. Jianlin Li and Dan Sweeney are also acknowledged for their helpful comments on earlier draft of the manuscript.

References

[1] L. Lu, X. Han, J. Li, J. Hua, M. Ouyang, A review on the key issues for lithium-ion battery management in electric vehicles, Journal of power sources 226 (2013) 272–288. doi:https://doi.org/10.1016/j.jpowsour.2012.10.060.

[2] M. Berecibar, I. Gandiaga, I. Villarreal, N. Omar, J. Van Mierlo, P. Van den Bossche, Critical review of state of health estimation methods of li-ion batteries for real applications, Renewable and Sustainable Energy Reviews 56 (2016) 572–587. doi:https://doi.org/10.1016/j.rser.2015.11.042.

[3] R. Huggins, Advanced Batteries: Materials Science Aspects, Springer Science & Business Media, 2008.

[4] Y. Xing, W. He, M. Pecht, K. L. Tsui, State of charge estimation of lithium-ion batteries using the open-circuit voltage at various ambient temperatures, Applied Energy 113 (2014) 106–115. doi:https://doi.org/10.1016/j.apenergy.2013.07.008.

[5] H. He, X. Zhang, R. Xiong, Y. Xu, H. Guo, Online model-based estimation of state-of-charge and open-circuit voltage of lithium-ion batteries in electric vehicles, Energy 39 (1) (2012) 310–318. doi:https://doi.org/10.1016/j.energy.2012.01.009.

[6] L. Kang, X. Zhao, J. Ma, A new neural network model for the state-of-charge estimation in the battery degradation process, Applied Energy 121 (2014) 20–27. doi:https://doi.org/10.1016/j.apenergy.2014.01.066.

[7] A. Hsieh, S. Bhadra, B. Hertzberg, P. Gjeltema, A. Goy, J. W. Fleischer, D. A. Steingart, Electrochemical-acoustic time of flight: in operando correlation of physical dynamics with battery charge and health, Energy & environmental science 8 (5) (2015) 1569–1577. doi:https://doi.org/10.1039/C5EE00111K.

[8] G. Davies, K. W. Knehr, B. Van Tassell, T. Hodson, S. Biswas, A. G. Hsieh, D. A. Steingart, State of charge and state of health estimation using electrochemical acoustic time of flight analysis, Journal of The Electrochemical Society 164 (12) (2017) A2746. doi:https://doi.org/10.1149/2.1411712jes.

[9] L. Gold, T. Bach, W. Virsik, A. Schmitt, J. Müller, T. E. Staab, G. Sextl, Probing lithium-ion batteries' state-of-charge using ultrasonic transmission–concept and laboratory testing, Journal of Power Sources 343 (2017) 536–544. doi:https://doi.org/10.1016/j.jpowsour.2017.01.090.

[10] P. Ladpli, F. Kopsaftopoulos, F.-K. Chang, Estimating state of charge and health of lithium-ion batteries with guided waves using built-in piezoelectric sensors/actuators, Journal of Power Sources 384 (2018) 342–354. doi:https://doi.org/10.1016/j.jpowsour.2018.02.056.

[11] H. Popp, M. Koller, S. Keller, G. Glanz, R. Klambauer, A. Bergmann, State estimation approach of lithium-ion batteries by simplified ultrasonic time-of-flight measurement, IEEE Access 7 (2019) 170992–171000. doi:https://doi.org/10.1109/ACCESS.2019.2955556.

[12] D. Rohrbach, E. Garcia-Tamayo, J. Potter, V. Martinez, M. Bernal, Nondestructive state-of-charge assessment of lithium-ion batteries using quantitative ultrasound spectroscopy, in: 2021 IEEE International Ultrasonics Symposium (IUS), IEEE, 2021, pp. 1–4. doi:https://doi.org/10.1109/IUS52206.2021.9593566.

[13] R. Copley, D. Cumming, Y. Wu, R. Dwyer-Joyce, Measurements and modelling of the response of an ultrasonic pulse to a lithium-ion battery as a precursor for state of charge estimation, Journal of Energy Storage 36 (2021) 102406. doi:https://doi.org/10.1016/j.est.2021.102406.

[14] C. Bommier, W. Chang, J. Li, S. Biswas, G. Davies, J. Nanda, D. Steingart, Operando acoustic monitoring of sei formation and long-term cycling in nmc/sigr composite pouch cells, Journal of The Electrochemical Society 167 (2) (2020) 020517.

[15] Y. S. Zhang, A. N. Pallipurath Radhakrishnan, J. B. Robinson, R. E. Owen, T. G. Tranter, E. Kendrick, P. R. Shearing, D. J. Brett, In situ ultrasound acoustic measurement of the lithium-ion battery electrode drying process, ACS Applied Materials & Interfaces 13 (30) (2021) 36605–36620. doi:https://doi.org/10.1021/acsami.1c10472.

[16] H. Li, Z. Zhou, Numerical simulation and experimental study of fluid-solid coupling-based air-coupled ultrasonic detection of stomata defect of lithium-ion battery, Sensors 19 (10) (2019) 2391. doi:https://doi.org/10.3390/s19102391.

[17] J. B. Robinson, R. E. Owen, M. D. Kok, M. Maier, J. Majasan, M. Braglia, R. Stocker, T. Amietszajew, A. J. Roberts, R. Bhagat, et al., Identifying defects in li-ion cells using ultrasound acoustic measurements, Journal of The Electrochemical Society 167 (12) (2020) 120530. doi:https://doi.org/10.1149/1945-7111/abb174.

[18] J. G. Swallow, W. H. Woodford, F. P. McGrogan, N. Ferralis, Y.-M. Chiang, K. J. Van Vliet, Effect of electrochemical charging on elastoplastic properties and fracture toughness of Li_XCoO_2, Journal of the electrochemical society 161 (11) (2014) F3084. doi:https://doi.org/10.1149/2.0141411jes.

[19] Y. Qi, L. G. Hector, C. James, K. J. Kim, Lithium concentration dependent elastic properties of battery electrode materials from first principles calculations, Journal of The Electrochemical Society 161 (11) (2014) F3010. doi:https://doi.org/10.1149/2.0031411jes.

[20] B. Sood, M. Osterman, M. Pecht, Health monitoring of lithium-ion batteries, in: 2013 IEEE Symposium on Product Compliance Engineering (ISPCE), IEEE, 2013, pp. 1–6. doi:https://doi.org/10.1109/ISPCE.2013.6664165.

[21] Y. Wu, Y. Wang, W. K. Yung, M. Pecht, Ultrasonic health monitoring of lithium-ion batteries, Electronics 8 (7) (2019) 751. doi:https://doi.org/10.3390/electronics8070751.

[22] J.-Y. Kim, J.-H. Jo, J.-W. Byeon, Ultrasonic monitoring performance degradation of lithium ion battery, Microelectronics Reliability 114 (2020) 113859. doi:https://doi.org/10.1016/j.microrel.2020.113859.

[23] E. Larose, S. Hall, Monitoring stress related velocity variation in concrete with a 2×10^{-5} relative resolution using diffuse ultrasound, The Journal of the Acoustical Society of America 125 (4) (2009) 1853–1856. doi:https://doi.org/10.1121/1.3079771.

[24] O. I. Lobkis, R. L. Weaver, Coda-wave interferometry in finite solids: Recovery of P-to-S conversion rates in an elastodynamic billiard, Physical review letters 90 (25) (2003) 254302. doi:https://doi.org/10.1103/PhysRevLett.90.254302.

[25] N. Maeda, A method for reading and checking phase times in autoprocessing system of seismic wave data, Zisin 38 (1985) 365–379.

[26] D. Barnard, G. Dace, O. Buck, Acoustic harmonic generation due to thermal embrittlement of Inconel 718, Journal of Nondestructive Evaluation 16 (2) (1997) 67–75. doi:https://doi.org/10.1007/BF02683879.

[27] N. Nitta, F. Wu, J. T. Lee, G. Yushin, Li-ion battery materials: present and future, Materials today 18 (5) (2015) 252–264. doi:https://doi.org/10.1016/j.mattod.2014.10.040.

[28] R. Jung, M. Metzger, F. Maglia, C. Stinner, H. A. Gasteiger, Oxygen release and its effect on the cycling stability of $LiNi_xMn_yCo_zO_2$ (NMC) cathode materials for li-ion batteries, Journal of The Electrochemical Society 164 (7) (2017) A1361. doi:https://doi.org/10.1149/2.0021707jes.

[29] I. Landa-Medrano, A. Eguia-Barrio, S. Sananes-Israel, S. Lijó-Pando, I. Boyano, F. Alcaide, I. Urdampilleta, I. de Meatza, In situ analysis of NMC|graphite li-ion batteries by means of complementary electrochemical methods, Journal of The Electrochemical Society 167 (9) (2020) 090528. doi:https://doi.org/10.1149/1945-7111/ab8b99.

[30] R. Yadav, D. Pandey, Ultrasonic properties at the nanoscale in some metals, Materials Letters 59 (5) (2005) 564–569. doi:https://doi.org/10.1016/j.matlet.2004.10.046.

[31] O. Dolotko, A. Senyshyn, M. Mühlbauer, K. Nikolowski, H. Ehrenberg, Understanding structural changes in nmc li-ion cells by in situ neutron diffraction, Journal of Power Sources 255 (2014) 197–203. doi:https://doi.org/10.1016/j.jpowsour.2014.01.010.

[32] K. Märker, P. J. Reeves, C. Xu, K. J. Griffith, C. P. Grey, Evolution of structure and lithium dynamics in $LiNi_{0.8}Mn_{0.1}Co_{0.1}O_2$ (NMC811) cathodes during electrochemical cycling, Chemistry of Materials 31 (7) (2019) 2545–2554. doi:10.1021/acs.chemmater.9b00140.

[33] X. Wu, B. Song, P.-H. Chien, S. M. Everett, K. Zhao, J. Liu, Z. Du, Structural evolution and transition dynamics in lithium ion battery under fast charging: An operando neutron diffraction investigation, Advanced Science 8 (21) (2021) 2102318. doi:https://doi.org/10.1002/advs.202102318.

[34] R. Essehli, A. Parejiya, N. Muralidharan, C. J. Jafta, R. Amin, M. B. Dixit, Y. Bai, J. Liu, I. Belharouak, Hydrothermal synthesis of Co-free NMA cathodes for high performance Li-ion batteries, Journal of Power Sources 545 (2022) 231938. doi:https://doi.org/10.1016/j.jpowsour.2022.231938.

[35] N. Muralidharan, R. Essehli, R. P. Hermann, R. Amin, C. Jafta, J. Zhang, J. Liu, Z. Du, H. M. Meyer III, E. Self, et al., Lithium Iron Aluminum Nickelate, $LiNi_xFe_yAl_zO_2$−new sustainable cathodes for next-generation cobalt-free li-ion batteries, Advanced Materials 32 (34) (2020) 2002960. doi:https://doi.org/10.1002/adma.202002960.

[36] L. Geng, J. Liu, D. L. Wood III, Y. Qin, W. Lu, C. J. Jafta, Y. Bai, I. Belharouak, Probing thermal stability of Li-ion battery Ni-rich layered oxide cathodes by means of operando gas analysis and neutron diffraction, ACS Applied Energy Materials 3 (7) (2020) 7058–7065. doi:https://doi.org/10.1021/acsaem.0c01105.

[37] D. Mohanty, J. Li, S. C. Nagpure, D. L. Wood, C. Daniel, Understanding the structure and structural degradation mechanisms in high-voltage, lithium-manganese–rich lithium-ion battery cathode oxides: A review of materials diagnostics, MRS Energy & Sustainability 2. doi:https://doi.org/10.1557/mre.2015.16.

[38] D. Mohanty, K. Dahlberg, D. M. King, L. A. David, A. S. Sefat, D. L. Wood, C. Daniel, S. Dhar, V. Mahajan, M. Lee, et al., Modification of Ni-rich FCG NMC and NCA cathodes by atomic layer deposition: preventing surface phase transitions for high-voltage lithium-ion batteries, Scientific reports 6 (1) (2016) 1–16. doi:https://doi.org/10.1038/srep26532.